J Mater Sci (2026) 61:10113–10130

Chemical routes to materials

Exploring the role of hydrolyzed Nb_2O_5 surfaces in manganese ion adsorption

Allef Leite[1,2], Jeferson Almeida Dias[3], Gelson Tavares da Silva[4], Rodrigo Leandro Bonifácio[5], Caue Ribeiro[1], Vagner Romito de Mendonça[6], and Tania Regina Giraldi[7,*]

[1] *Nanotechnology Laboratory for Agribusiness, Embrapa Instrumentation, Rua XV de Novembro, 1.452, São Carlos, SP 13560-970, Brazil*
[2] *São Carlos Institute of Chemistry, University of São Paulo, Avenida Trabalhador São Carlense, 400, São Carlos, SP 13566-590, Brazil*
[3] *School of Applied Sciences, Metallurgy Laboratory, State University of Campinas, Rua Pedro Zaccaria, 1.300, Limeira, SP 13484-350, Brazil*
[4] *Department of Chemistry, Interdisciplinary Laboratory of Eletrochemistry and Ceramics, Federal University of São Carlos, Rodovia Washington Luís, Km 235, São Carlos, SP 13565-905, Brazil*
[5] *Chemical Analyses Laboratory, Poços de Caldas Laboratory, Brazilian Nuclear Energy Commission, Rodovia Poços de Caldas/Andradas Km 13, Poços de Caldas, MG 37719-005, Brazil*
[6] *Federal Institute of Education, Science and Technology of São Paulo, Avenida João Olímpio de Oliveira, 1.561, Itapetininga, SP 18202-000, Brazil*
[7] *Institute of Science and Technology, Federal University of Alfenas, Rodovia José Aurélio Vilela, 1.999, Poços de Caldas, MG 37715-400, Brazil*

Received: 29 July 2025
Accepted: 17 February 2026
Published online: 10 March 2026

ABSTRACT

This work investigates the adsorption of Mn^{2+} ions on hydrothermally synthesized Nb_2O_5 nanoparticles obtained via an oxidant peroxo method, with particular emphasis on the role of functional groups present on the nanoparticle surface. Orthorhombic Nb_2O_5 was formed at a mild temperature (100 °C), yielding nanocrystalline particles with high colloidal stability and a strongly negative surface charge. FTIR and zeta potential analyses reveal a carbonyl and hydroxyl-rich surface that promotes electrostatic attraction toward Mn^{2+} species. Adsorption experiments demonstrate rapid Mn^{2+} uptake, reaching equilibrium within minutes, with kinetics best described by a pseudo-first-order model, indicating a physisorption-dominated process. Equilibrium data are best fitted by the Freundlich and Redlich–Peterson isotherms, reflecting surface heterogeneity and multilayer adsorption, with an experimental adsorption capacity approaching 116.67 mg g^{-1}. These findings demonstrate that hydrolyzed Nb_2O_5 is an efficient and tunable adsorbent for Mn^{2+} removal, offering strong potential for water treatment and environmental remediation applications.

Handling Editor: Ivo Teixeira.

Address correspondence to E-mail: tania.giraldi@unifal-mg.edu.br

https://doi.org/10.1007/s10853-026-12458-9

GRAPHICAL ABSTRACT

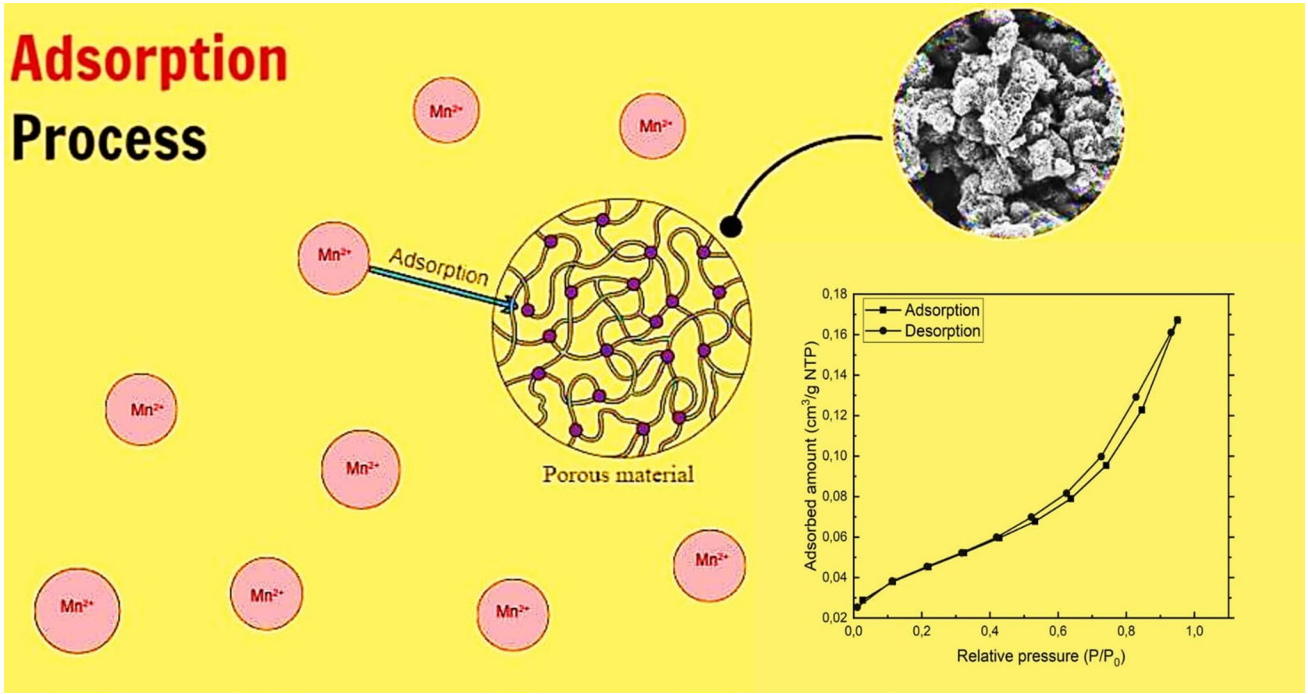

Introduction

Inorganic materials play a crucial role in a wide range of technological applications. Precise tuning of their surface properties is essential to optimize their overall performance. A detailed understanding and control of these properties can significantly enhance their effectiveness in photocatalytic, thermocatalytic, and adsorption processes. Among these materials, niobium pentoxide (Nb_2O_5) has attracted considerable attention in catalysis and adsorption due to its distinctive characteristics, including polymorphism and surface chemistry [1, 2]. Nb_2O_5 is of notable technological relevance, owing to its unique chemical and physical properties [3]. These attributes render it a highly promising material for diverse applications, such as gas sensing devices [4], photovoltaic solar cells [5], electrochromic systems [6], supercapacitors [7, 8], and adsorbent materials [9, 10]. In addition, niobium oxides are integral to various catalytic processes [11, 12], functioning either as the primary active phase [13] or as a support material that enhances overall catalytic performance [12, 13]. A remarkable feature of Nb_2O_5 is the coexistence of Brønsted and Lewis acid sites, which endow it with amphoteric behavior, allowing it to act as either an acid or a base depending on the reaction medium. When Nb_2O_5 exhibits Brønsted acidity, the proton-donating groups are commonly represented as protons (H^+) bonded to surface oxygen atoms, forming hydroxyl groups (-OH). Basic sites are typically attributed to oxygen ions (O^-), which arise either through proton dissociation or via the dehydration of adjacent surface hydroxyl groups [14]. These intrinsic acid–base properties significantly influence the material's adsorption behavior, impacting reaction mechanisms and enhancing selectivity in various chemical processes. The versatility of Nb_2O_5, driven by its structural and electronic properties, continues to make it a subject of extensive research. In the present work, we focus on its adsorption potential for manganese. Although manganese occurs naturally in soil, air, water, and food and is an essential trace element involved in regulating metabolic processes in living organisms [15], both deficiency and excess can have deleterious effects, potentially causing severe harm or even death. This toxicity is primarily associated with the formation of complexes between manganese and enzyme functional groups within biological systems

[16]. Consequently, manganese is considered a relevant contaminant in water environments.

Various types of adsorbents have been reported in the literature, specifically for the adsorption of Mn^{2+} ions. Kan et al.[17] investigated the adsorption of Mn^{2+} onto iron oxide-coated sand adsorbents under varying pH and temperature conditions. Equilibrium studies indicated that adsorption followed both Langmuir and Freundlich isotherms, suggesting monolayer coverage and surface heterogeneity, with good affinity for Mn^{2+} (b = 1.656 L mg^{-1}, Q_{max} = 0.884 mg g^{-1}). Kinetic data best fit the pseudo-second-order model, implying a chemisorption-controlled process. Fikri et al. [18] examined the impact of different thicknesses of zeolite and activated carbon media adsorbents on reducing manganese concentrations in wastewater from nondestructive testing processes. They varied the adsorbent thickness between 40 and 80 cm and achieved a maximum Mn^{2+} removal efficiency of 80%. Radoykova et al. [19] explored the removal of Mn^{2+} ions onto hydrolyzed lignocellulosic materials (HL) and alkaline-treated hydrolyzed lignin (AAHL) derived from paulownia, wheat straw, and maize. Adsorption followed the Langmuir model, indicating monolayer adsorption with parameters dependent on the material and treatment. The adsorption capacity (Q_{max}) of HL materials was approximately twice that of AAHL samples, highlighting the influence of material structure. Specific surface area (S_0) and adsorption capacity per unit surface (q_s) were analyzed, with pAAHL(p) exhibiting the highest q_s (0.58 mg m^{-2}) despite having the lowest surface area.

Although Nb_2O_5 has been incorporated into composites or mixed oxides for Mn^{2+} removal [20–22], existing studies do not isolate the intrinsic contribution of Nb_2O_5 itself, nor do they examine how hydrolysis-driven surface reconstruction affects its adsorption behavior. Most reports employ Nb_2O_5 as part of multi-component matrices, making it difficult to discern how surface hydroxylation, acid–base site distribution, or crystallinity influence Mn^{2+} uptake [23]. To the best of our knowledge, no work has systematically evaluated Mn^{2+} adsorption on hydrothermally treated and hydrolyzed Nb_2O_5 obtained via an oxidant peroxo route, nor correlated the degree of surface hydroxylation with adsorption capacity. In this study, we address these gaps by isolating the role of hydrolyzed Nb_2O_5 surfaces and analyzing how controlled surface reconstruction affects Mn^{2+} affinity. The ability to manipulate the surface via structural modifications and maintain hydroxyl groups ought to enhance the material's affinity for Mn^{2+} and the performance of the adsorption system. Several synthesis methods have been studied for the preparation of Nb_2O_5, including sol–gel, combustion, polymeric precursors, microwave-assisted hydrothermal reaction [24], and solvothermal treatment [7]. However, the hydrothermal treatment method stands out for promoting crystallization, modifying surface properties [9, 25, 26], and most importantly, enhancing surface hydroxylation [11, 13, 18], which makes Nb_2O_5 a promising adsorbent for cationic species. The oxidant peroxo method (OPM) is notable for its simplicity and effectiveness. This approach involves forming a metal complex with hydrogen peroxide, followed by precipitation or crystallization under hydrothermal conditions, thereby avoiding the use of halides or organic solvents that could influence the material's formation or surface characteristics. The preference for OPM arises from its ability to conduct reactions at relatively mild temperatures (100–200 °C), thereby allowing precise control over nanoparticle surface chemistry and morphology. These moderate conditions help preserve surface hydroxyl groups, thereby maintaining acidic sites favorable for adsorption. Although a wide range of adsorbents has been reported for Mn^{2+} removal, the selection of Nb_2O_5 in this study is justified by its distinctive surface properties. Unlike many conventional adsorbents, Nb_2O_5 exhibits both Brønsted and Lewis acid sites, enabling multiple types of interactions with adsorbed species. Moreover, its highly hydroxylated surface enhances ionic adsorption, increasing its affinity for Mn^{2+} in aqueous solutions [27]. The combination of these intrinsic properties, together with the ability to finely tune surface characteristics through synthesis, renders Nb_2O_5 a highly promising material for heavy metal removal applications.

Given that charged contaminants such as Mn^{2+} cations preferentially adsorb onto surfaces with opposite charges [14], the adsorptive potential of Nb_2O_5 for Mn^{2+} in aqueous solutions was systematically investigated. The structural, morphological, and surface properties of the nanoparticles were evaluated. Subsequently, the kinetics and adsorption isotherms of Mn^{2+} ions were determined, providing insights into adsorption rates, maximum capacities, adsorbent–adsorbate affinity, and surface

heterogeneity. This comprehensive assessment provides valuable information for the design of environmentally friendly, cost-effective systems for Mn^{2+} removal, addressing the growing concern about heavy metal contamination, particularly in industrialized regions [28]. By understanding the interplay among synthesis conditions, structural characteristics, and adsorption behavior, the full potential of Nb_2O_5 as an adsorbent for heavy metal remediation can be realized.

Experimental

Synthesis of Nb_2O_5 and hydrothermal treatment

The synthesis of Nb_2O_5 nanoparticles was carried out by dispersing 2 g of ammonium niobium oxalate ($[Nb(C_2O_4)_2(NH_3)_2].nH_2O$, CBMM, Brazil) in distilled water, followed by the addition of 4 mL of H_2O_2 (30% v/v, Dinâmica). The resulting solution was transferred to a stainless steel hydrothermal reactor and heated at 100 °C for different reaction times (4, 12, and 24 h). After completion of the hydrothermal process, the products were collected and thoroughly washed with distilled water to remove residual species. The samples were then dried in an oven at 80 °C for 24 h to ensure complete moisture removal. Finally, the obtained powders were ground in an agate mortar and labeled as xNbT, where x corresponds to the synthesis time and T to the reaction temperature (4Nb100, 12Nb100, and 24Nb100).

Characterizations

The crystallographic structure of the samples was analyzed using a Shimadzu XRD-6000 diffractometer operated at 40 kV and 30 mA, equipped with a graphite monochromator. X-ray diffraction patterns were collected over a 2θ range of 15° to 60°, using a step size of 0.02°. The average crystallite size (D) was estimated using the Scherrer equation [29], based on the (001) reflection of the orthorhombic Nb_2O_5 phase. Peak deconvolution was performed using a Lorentzian function to accurately determine the full width at half maximum (FWHM) of each diffraction peak. A cubic silicon standard (space group $Fd\bar{3}m$) was measured under the same experimental conditions to correct for instrumental broadening effects, following standard procedures [30]. The (111) reflection of the silicon pattern was fitted using a Gaussian function, as it provided the best fit for this reference sample. The proportions of the peak areas for each phase relative to the total were monitored to identify possible trends in phase transformation as a function of the hydrothermal treatment period. For this purpose, the XRD patterns were refitted using Gaussian functions, enabling peak deconvolution and accurate integration. The tendencies for phase evolution were then monitored using a methodology similar to that used in the literature for crystallinity estimation and phase proportion [31, 32]. Additionally, to evaluate sample purity, semiquantitative elemental analyses were performed by X-ray fluorescence using a Shimadzu EDX-720 instrument.

To evaluate the thermal stability of the samples, thermogravimetric analysis (TGA) was performed to monitor mass changes as a function of temperature. In addition, differential scanning calorimetry (DSC) was employed to record heat flow associated with thermal events. The measurements were carried out under controlled temperature conditions using a STA 449 F3 Jupiter® analyzer over a temperature range of 20 to 800 °C. A constant heating rate of 10 °C min^{-1} was applied, and the experiments were conducted under a synthetic air atmosphere. Both endothermic and exothermic events were identified and recorded during the thermal analysis.

Fourier transform infrared spectroscopy (FTIR) was employed to identify functional groups present in the samples. The analyses were performed using an Agilent® Cary 630 FTIR spectrometer operating in attenuated total reflectance (ATR) mode, over the spectral range of 4000–650 cm^{-1}, with a resolution of 4 cm^{-1}.

N_2 adsorption–desorption measurements were used to investigate the textural and morphological properties of the samples and determine the specific surface area and porosity. Prior to analysis, the samples were pre-dried in an oven at 105 °C for 24 h to remove residual moisture. Subsequently, vacuum degassing was performed at 105 °C for 3 h using a Micromeritics® VacPrep 061 system. Nitrogen adsorption measurements were then carried out by varying the N_2 pressure from 7 to 635 mmHg.

The morphology of the nanoparticles was examined by field emission scanning electron microscopy (FE-SEM) using a JEOL JSM-6701F microscope. Particle size and structural features were further analyzed by transmission electron microscopy (TEM) using

an FEI Tecnai G2 F20 microscope operated at 200 kV and equipped for high-resolution TEM (HRTEM) and energy-dispersive X-ray spectroscopy (EDS). The images were recorded with a Ceta 16 M CMOS camera at 4096 × 4096 pixels (Thermo Fisher Scientific).

The surface charge characteristics of the samples were investigated by zeta potential measurements using a Malvern® Zetasizer Nano. Aqueous suspensions were prepared at a concentration of 1 mg L^{-1} by dispersing the samples in deionized water. Initially, all samples were analyzed at their natural pH (5.8), which remained constant without further adjustment. Subsequently, the sample 24Nb100 was selected for a more detailed pH-dependent study. For this purpose, suspensions were prepared by dispersing 1 mg of the sample in 10 mL of deionized water, followed by sonication using a Branson digital sonifier. The pH of the suspensions was adjusted to approximately 3 to 9.5 using aqueous solutions of sodium hydroxide (NaOH, Synth®) and hydrochloric acid (HCl, Synth®). This procedure enabled the evaluation of the zeta potential behavior of the samples under different pH conditions.

The adsorption behavior of the samples toward Mn^{2+} ions was investigated through a series of experiments performed in triplicate under controlled agitation at ambient temperature. Four sets of experiments were conducted: evaluation of the effect of Nb_2O_5 nanoparticle concentration, pH, adsorption kinetics, and adsorption isotherms.

Mn^{2+} adsorption tests for Nb_2O_5

The adsorption capacity of the Nb_2O_5 samples, prepared by hydrothermal treatment at 100 °C for different durations (4, 12, and 24 h), was evaluated for the removal of Mn^{2+} at ambient temperature. Sample solutions contained 2.0 mg L^{-1} Nb_2O_5 and 10 mg L^{-1} Mn^{2+}. To investigate the effect of adsorbent concentration, Nb_2O_5 was tested at 0.5, 1.0, 1.5, and 2.0 mg L^{-1} by adding 0.005, 0.01, 0.015, and 0.02 g of Nb_2O_5, respectively, to 10 mL of solution. Subsequently, adsorption experiments were carried out to investigate the effect of pH on Mn^{2+} adsorption, employing a fixed contact time of 1 h and suspensions containing 2.0 mg L^{-1} adsorbent and 10 mg L^{-1} adsorbate, with pH values ranging from 3.5 to 7.8. Adsorption kinetics were studied by contacting 0.02 g of Nb_2O_5 with 10 mL of a 10 mg L^{-1} Mn^{2+} solution for different contact times (1, 3, 5, 10, 20, 30, 40, 50, and 60 min). In comparison, adsorption isotherms were determined by dispersing a 2 g L^{-1} Nb_2O_5 suspension in Mn^{2+} solutions of varying concentrations (10, 15, 20, 50, 75, and 100 mg L^{-1}) for 60 min. After stirring, all suspensions were centrifuged, and the residual Mn^{2+} concentrations in the supernatants were determined using the high-resolution atomic absorption spectrometer (ContrAA® 300, Analytik Jena) with an air/acetylene flame.

Kinetic and isotherm modeling

Adsorption kinetics were evaluated using pseudo-first-order and pseudo-second-order models in their nonlinear forms. The pseudo-first-order model [33] assumes that the adsorption rate is proportional to the number of unoccupied sites and is expressed as:

$$Q_t = Q_e(1 - e^{-k_1 t}) \tag{1}$$

where Q_t (mg g^{-1}) is the amount adsorbed at time t (min), Q_e (mg g^{-1}) is the equilibrium adsorption capacity, and k_1 (min^{-1}) is the pseudo-first-order rate constant.

The pseudo-second-order model [33] assumes that chemisorption is the rate-limiting step and is given by:

$$Q_t = \frac{k_2 Q_e^2 t}{1 + k_2 Q_e t} \tag{2}$$

where k_2 (g mg^{-1} min^{-1}) is the pseudo-second-order rate constant.

Equilibrium adsorption data were analyzed using Langmuir, Freundlich, Temkin, and Redlich–Peterson isotherm models. The Langmuir model [34] assumes monolayer adsorption on a homogeneous surface with finite identical sites and is expressed as:

$$Q_e = \frac{Q_{max} K_L C_e}{1 + K_L C_e} \tag{3}$$

where Q_{max} (mg g^{-1}) is the maximum monolayer adsorption capacity, K_L (L mg^{-1}) is the Langmuir affinity constant, and C_e (mg L^{-1}) is the equilibrium concentration.

The Freundlich model [35] describes adsorption on heterogeneous surfaces and is given by:

$$Q_e = K_F C_e^{1/n} \tag{4}$$

where K_F ((mg g^{-1})(L mg^{-1})$^{(1/n)}$) is the Freundlich constant related to adsorption capacity and n is the heterogeneity factor.

The Temkin model [36] accounts for adsorbate–adsorbent interactions and assumes a linear decrease in adsorption heat with surface coverage, expressed as:

$$Q_e = Bln(A_T C_e) \quad (5)$$

where A_T (L g^{-1}) is the Temkin equilibrium binding constant and B (kJ mol^{-1}) is related to the heat of adsorption.

The Redlich–Peterson model [36] combines features of Langmuir and Freundlich isotherms and is expressed as:

$$Q_e = \frac{K_R C_e}{1 + a_R C_e^g} \quad (6)$$

where K_R (L g^{-1}) and a_R (L mg^{-1})^g are model constants and g is an exponent between 0 and 1.

All kinetic and isotherm parameters were obtained by nonlinear regression using least-squares minimization, avoiding linearization-induced bias. The quality of fit was assessed using the coefficient of determination (R^2) and the chi-square statistic (χ^2).

Results and discussion

Characterizations

X-ray diffraction (XRD) was used to investigate the crystalline structure of the adsorbents. Figure 1 shows the X-ray diffractograms of the samples obtained at 100 °C, with varying hydrothermal treatment times.

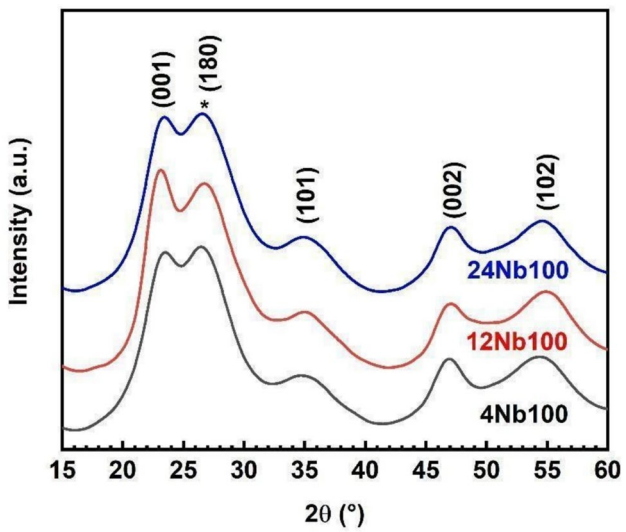

Figure 1 X-ray diffraction pattern of Nb_2O_5 nanoparticles.

The diffraction patterns of the samples are notably similar and are consistent with the orthorhombic phase of Nb_2O_5, as established by the Joint Committee on Powder Diffraction Standards (ICDD-JCPDS, n° 27–1003) [23]. The formation of the orthorhombic structure is consistent with literature reports, indicating that these phases are preferentially formed under high-temperature, low-pressure conditions. Interestingly, in this study, the orthorhombic phase was obtained at mild temperatures. Moreover, the specific synthesis conditions employed may have favored its formation. The broad peak around $2\theta \cong 26°$, marked with an asterisk in Fig. 1, corresponds to the combination of the hydrated niobium oxide peak and the (180) reflection of the orthorhombic Nb_2O_5 phase. The presence of hydrated niobium oxide is consistent with the literature on niobium oxide synthesis under mild conditions [14].

The diffraction peaks are also broadened, suggesting the presence of small crystallites. This is characteristic of nanocrystalline materials, with individual crystal sizes in the range of 10–200 nm, leading to XRD peak broadening [23]. To confirm this observation, the average crystallite size (D) was estimated. Figure S1 (Supplementary Information) presents deconvolution graphs used for accurate measurement of peak broadening. The results showed that samples 4Nb100, 12Nb100, and 24Nb100 exhibited D values of 2.5 nm, 3.4 nm, and 2.8 nm, respectively, confirming their nanocrystalline nature. Interestingly, the crystallite sizes were consistent across all samples, regardless of synthesis time, suggesting that crystal formation was not significantly affected by variation in synthesis time and highlighting the robustness and reproducibility of the preparation method, even for short synthesis durations. Moreover, the integrated peak areas of $Nb_2O_5.nH_2O$ relative to the total peak area were determined to be 9.7%, 10.5%, and 9.6% for samples 4Nb100, 12Nb100, and 24Nb100, respectively. These results indicate that the $Nb_2O_5.nH_2O$ phase remained basically constant during the hydrothermal treatment, as reflected by the nearly unchanged relative peak areas. Thus, this result demonstrates that the proportion of the hydrated phase does not affect differences in adsorption capability among the samples, as they remain nearly constant. Importantly, these percentages represent only trends in phase evolution inferred from variations in sample peak areas and do not correspond directly to phase quantification.

Table 1 Semi-quantitative elemental analyses of samples prepared with different periods of hydrothermal treatment

Element (%)	4Nb100	12Nb100	24Nb100
Nb	99.13 ± 0.20	99.39 ± 0.20	99.30 ± 0.20
Cl	0.56 ± 0.05	0.51 ± 0.05	0.50 ± 0.05
Ta	0.24 ± 0.03	–	–
Ga	0.05 ± 0.01	0.03 ± 0.01	0.05 ± 0.01
Pt	0.02 ± 0.02	–	–
Cu	–	0.07 ± 0.01	0.07 ± 0.01
Zr	–	–	0.08 ± 0.01

The elemental analyses of the samples performed by XRF are presented in Table 1. All three samples exhibited high purity, with more than 99.1 at.% composed of Nb, the main expected element. It is important to note that XRF does not detect elements lighter than sodium, and therefore, they are not quantified by this technique. Consequently, the actual elemental purity is implicitly higher than the reported values, since the Nb cations in the samples are bonded to oxygen anions to form Nb_2O_5, and XRF does not quantify oxygen. Minor signals from other elements were also detected and are attributed to trace impurities originating from the precursor and other reactants, as is common in chemical synthesis methods.

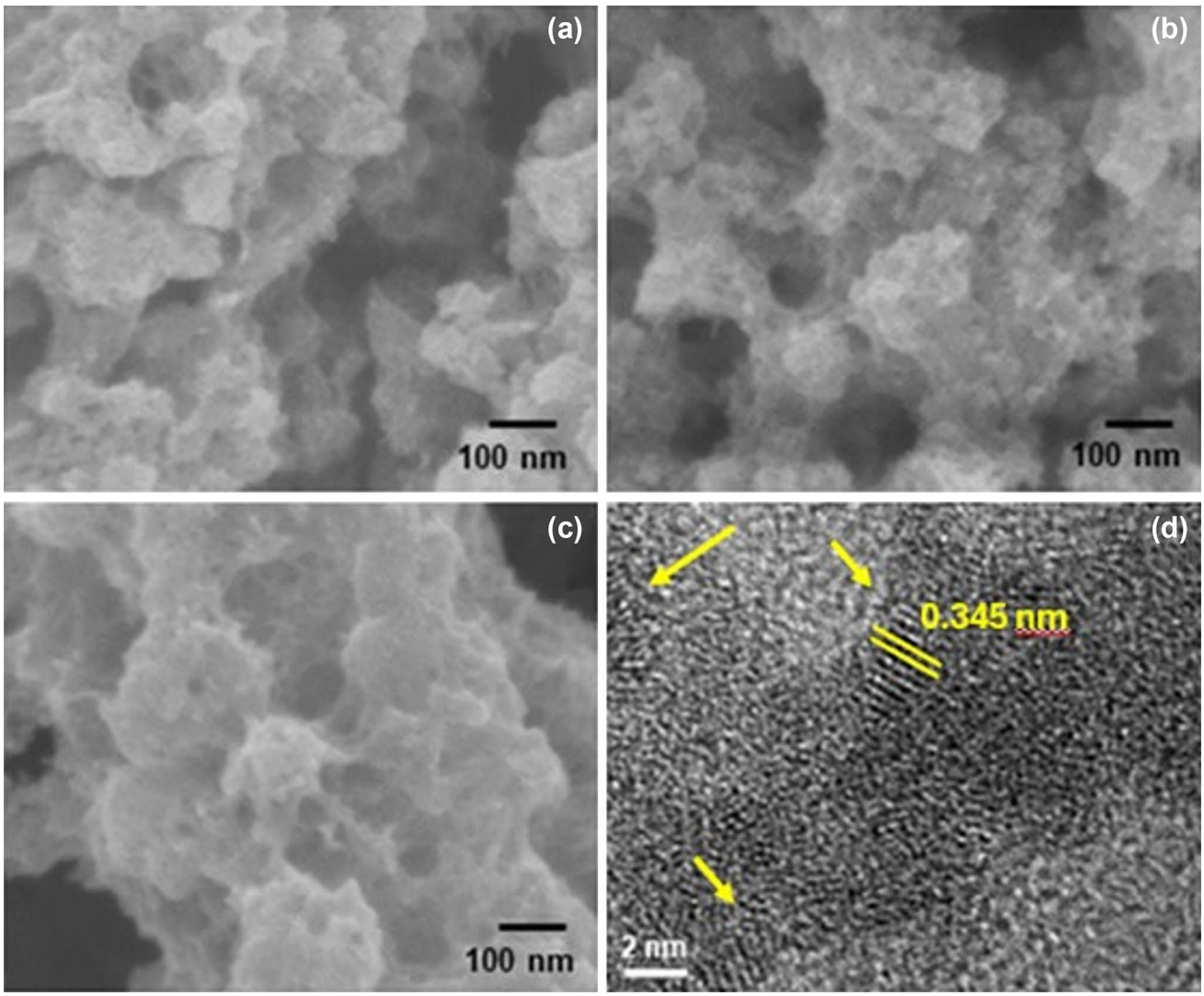

Figure 2 Field emission electron scanning microscopy images of Nb_2O_5 nanoparticles obtained by hydrothermal treatment at 100 °C for **a** 4, **b** 12, and **c** 24 h and **d** TEM image for the sample 24Nb100.

FE-SEM images of the samples treated for different durations support these results. Particles treated for 4, 12, and 24 h exhibited a spongy morphology, with some regions showing particles of spherical morphology. Figure 2 presents the HRTEM image of the 24Nb100 sample. The interplanar spacing of 0.345 nm corresponds to the (180) and (200) reflections observed in XRD at around 26°, confirming the material's crystalline structure. Additionally, the crystallite sizes observed in the HRTEM image (highlighted by yellow arrows) agree with those calculated from the Scherrer equation.

Thermal analysis (TG/DSC) was employed to evaluate the thermal stability of the Nb_2O_5 samples. Figure 3 presents the results for samples 4Nb100 (a) and 24Nb100 (b). The analysis revealed a common pattern of mass loss in all samples (Figure S2), characterized by a sharp decrease below approximately 500 °C. The initial mass loss, observed up to around 300 °C, is attributed to the removal of surface-adsorbed water. At higher temperatures, the release of coordinated water from the bulk and the evaporation of volatile species originating from the niobium ammoniacal precursor are observed [14]. No further significant mass losses were detected at even higher temperatures. All mass loss events were of considerable magnitude, suggesting that the produced Nb_2O_5 is predominantly non-stoichiometric and contains residual impurities from the precursor complex.

Three well-defined peaks are observed in the DSC data of the samples. The first peak, around 100 °C, is endothermic and corresponds to the evaporation of water present in the system. The second peak, at approximately 340 °C, likely indicates the removal of structurally bound water and residual synthesis by-products. The third peak, around 600 °C, suggests a modification of the material's structure, corresponding to the transition from the orthorhombic to an amorphous phase, followed by reformation of the orthorhombic structure with high crystallinity [37]. TG data (Fig. 3) show no mass change at this temperature, supporting the occurrence of an internal structural rearrangement.

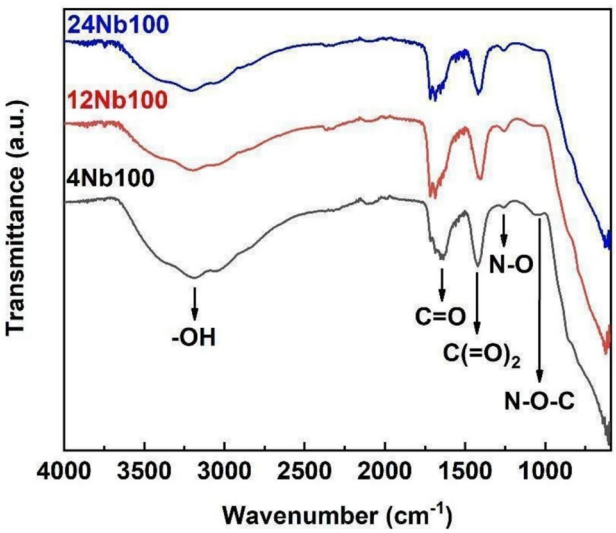

Figure 4 Fourier transform infrared spectroscopy spectrum of Nb_2O_5.

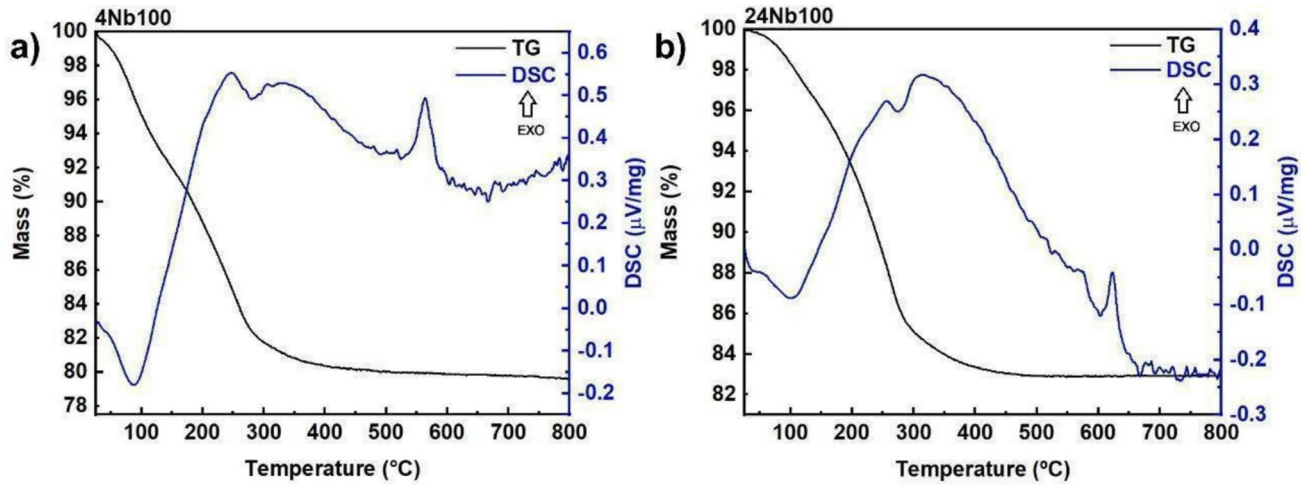

Figure 3 Thermal analysis (TGA/DSC) for samples **a** 4Nb100 and **b** 24Nb100.

To investigate the molecular structure and chemical interactions in Nb_2O_5, the samples were analyzed by FTIR, and the resulting spectra are shown in Fig. 4. The spectra reveal a broad absorption band with peaks between 3415 and 3183 cm^{-1}, indicating vibrations associated with OH groups. These OH groups likely arise from surface hydroxylation and are consistent with previous observations [14], suggesting significant interactions between niobium and hydroxyl groups on the particle surface. Moreover, Fig. 4 shows that increasing the hydrothermal treatment time reduces the intensity of this band, indicating the removal of surface hydroxyl groups.

Bands associated with functional groups from synthesis residues are also observed. The band at 1625 cm^{-1} corresponds to carbonyl groups (C = O), while the band at 1424 cm^{-1} is related to the oxalate ion ($C(=O)_2$). The band at 1252 cm^{-1} corresponds to the stretching of the N–O bond, possibly resulting from the oxidation of ammonia to NO_x groups. These bands are characteristic of the ammoniacal niobium precursor complex [14]. A band attributed to the Nb–O–C bond was also identified at 1068 cm^{-1} [14].

The surface area, porosity, and pore size distribution were analyzed using the Brunauer–Emmett–Teller (BET) and Barrett–Joyner–Halenda (BJH) methods. Figure 5 shows the nitrogen adsorption isotherm for the 24Nb100 sample. Similar analyses were performed for the 4Nb100 and 12Nb100 samples, which showed identical isotherm profiles (Figures S2 and S3). The isotherms are classified as Type IV according to IUPAC [38], indicative of the presence of mesopores and macropores in the material.

Table 2 BET surface area, pore volume, pore size, and zeta potential of samples subjected to hydrothermal treatment at 100 °C

Samples	BET surface area ($m^2\ g^{-1}$)	Pore volume ($cm^3\ g^{-1}$)	Average pore size (Å)	Zeta potential (mV)
4Nb100	206	0.17	36	−27.5
12Nb100	153	0.15	39	−34.9
24Nb100	126	0.15	44	−24.9

Table 2 presents the specific surface area, average pore size, and total pore volume of each sample. The average pore size is within the typical range for mesoporous materials (20–500 Å), indicating the presence of mesopores in the samples.

The specific surface area decreases with increasing hydrothermal treatment time, consistent with the increase in crystallite size. However, the longer treatment time did not lead to pore closure, as might be expected at higher temperatures. Table 2 also presents the zeta potential values of nanoparticle suspensions at pH 5.8. The samples exhibited zeta potentials below -24.9 mV, indicating high colloidal stability. This suggests that repulsive forces dominate over attractive van der Waals forces, favoring both particle dispersion in the solution and electrostatic attraction with positively charged ions [39]. The role of zeta potential in

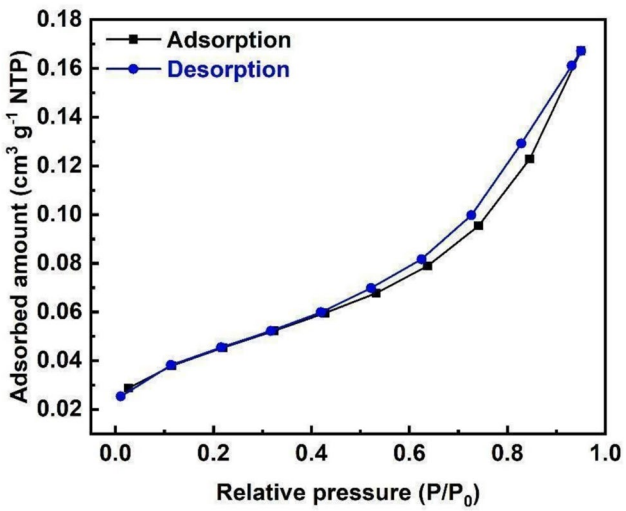

Figure 5 Nitrogen adsorption isotherm of 24Nb100.

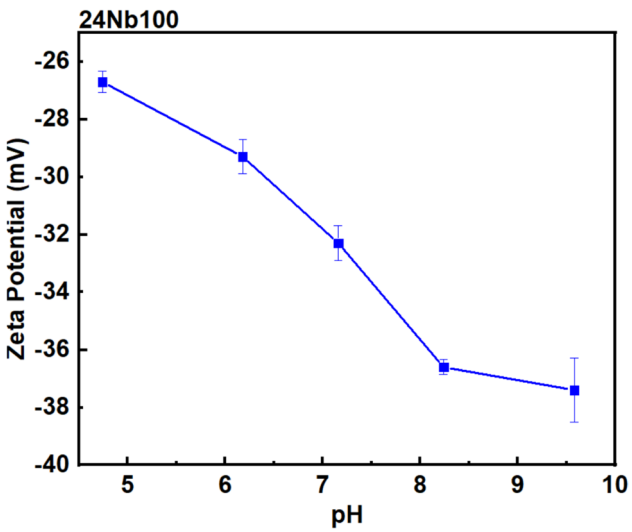

Figure 6 Zeta potential of the 24Nb100 sample varying pH in the range of 4 to 10.

adsorption on porous materials is particularly important. Adsorption involves multiple stages, including convective transport and diffusion within the pores, and suspension stability critically influences particle–solute interactions. Figure 6 shows a zeta potential study of the 24Nb100 suspension at varying pH values; the isoelectric point was not detected, suggesting that it may occur at lower pH values than those studied. Literature reports [14] indicate that the isoelectric point of Nb_2O_5 obtained via the peroxide oxidation method lies below pH 2.0. This characteristic is advantageous for potential applications, as it prevents particle aggregation and maintains a larger active surface area for adsorption and suspension stability. For Mn^{2+} removal, the negatively charged Nb_2O_5 surface electrostatically attracts and binds positively charged Mn^{2+} ions, enhancing adsorption efficiency.

Mn^{2+} adsorption on Nb_2O_5 nanoparticles

The adsorption capacity of the samples toward Mn^{2+} ions was evaluated. Adsorption experiments were initially conducted using the three Nb_2O_5 samples: 4Nb100, 12Nb100, and 24Nb100, to identify the sample with the highest Mn^{2+} removal in aqueous solution. Figure 7a shows the adsorption results. The 24Nb100 sample exhibited the highest Mn^{2+} removal (78.9%), compared to 4Nb100 (69.1%) and 12Nb100 (66.5%). Santos et al. [23] demonstrated that surface hydroxyl groups on Nb_2O_5 play a key role in the adsorption of charged species. In the present study, FTIR analysis (Fig. 4) confirmed the presence of surface hydroxyls in all samples. Furthermore, zeta potential measurements indicate values around -30 mV for all samples, suggesting strong electrostatic interactions with Mn^{2+} ions.

The superior adsorption capacity of 24Nb100 can be attributed to its larger mesopore size and greater accessible internal pore volume. Although the average pore diameters of 12Nb100 and 4Nb100 are within the mesoporous range (36–39 Å), the slightly larger pores of 24Nb100 (44 Å) reduce steric hindrance along the diffusion pathways, facilitating deeper penetration of solvated Mn^{2+} ions. The geometric descriptor, defined as the ratio of pore volume to BET surface area, indicates that 24Nb100 has a higher effective pore thickness (11.9 Å) than 12Nb100 (9.8 Å) and 4Nb100 (8.25 Å), reflecting a more open internal pore environment. This enhanced volumetric accessibility allows a larger fraction of the surface to actively participate in adsorption, demonstrating that, in this system, mesopore architecture and effective internal

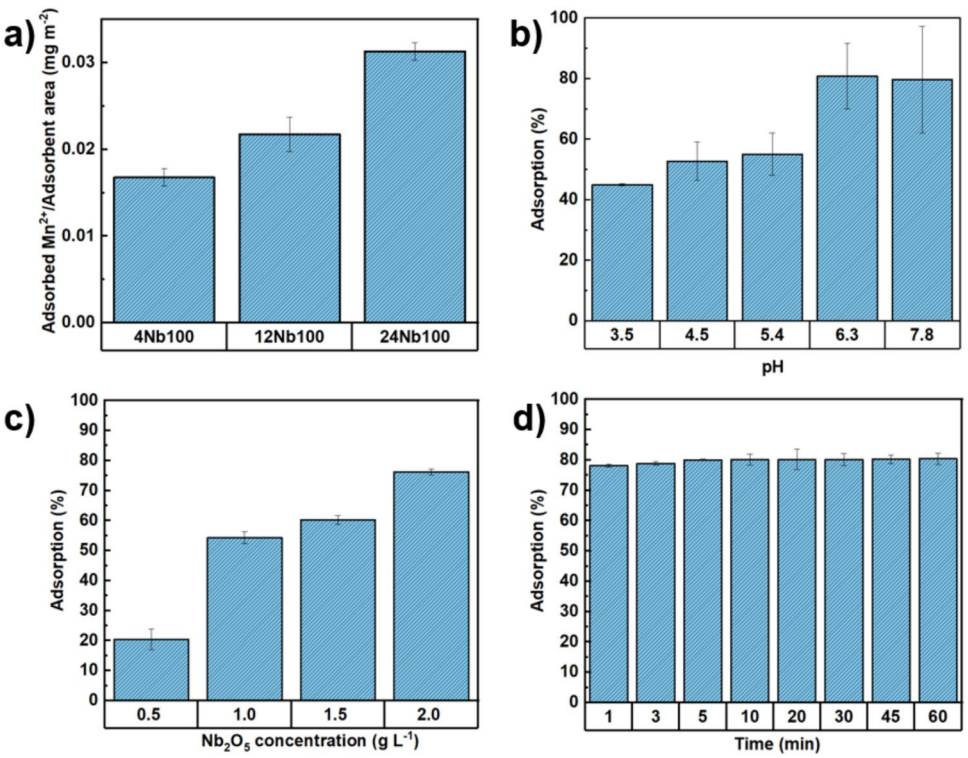

Figure 7 **a** Amount of Mn^{2+} adsorbed per adsorbent area for the 4Nb100, 12Nb100, and 24Nb100 samples, **b** Study of pH effect on Mn^{2+} adsorption for the 24Nb100 sample at pH 3.5, 4.5, 5.4, 6.3, and 7.8, **c** Study of particle concentration variation (0.5 g L^{-1}, 1.0 g L^{-1}, 1.5 g L^{-1}, and 2.0 g L^{-1}) for the 24Nb100 sample, and **d** Percentage of adsorption of the 24Nb100 sample varying contact time at 1, 3, 5, 10, 20, 30, 45, and 60 min.

volume govern adsorption performance more than absolute surface area. Consequently, the larger pores of 24Nb100 fully account for its higher Mn^{2+} uptake under the studied conditions [40].

Since the 24Nb100 sample exhibited the highest adsorption, it was selected for all subsequent experiments, including particle concentration, pH, adsorption kinetics, and isotherms. To evaluate the influence of pH on the adsorption performance of the 24Nb100 sample, experiments were conducted over a pH range of 3.5 to 7.8. The adsorption results are summarized in Fig. 7b, showing that the adsorption capacity increased from 44.9% at pH 3.5 to a maximum of 80.8% at pH 6.3. The enhanced adsorption at pH 5.4–6.3 can be attributed to the favorable surface charge of Nb_2O_5 under these conditions, which promotes electrostatic interactions with Mn^{2+} ions. Conversely, at pH values above 7.0, the adsorption efficiency decreased slightly (79.7% at pH 7.8), and the standard deviation increased markedly (17.6%), indicating a high degree of variability in the measurements. This behavior can be explained by the onset of $Mn(OH)_2$ precipitation at higher pH, which limits the reliability of adsorption measurements and underscores that pH 7.8 represents the upper practical limit for these studies. At highly acidic conditions (pH 3.5–4.5), adsorption was significantly lower (44.9–52.7%), reflecting the competition between H^+ ions and Mn^{2+} for active sites on the Nb_2O_5 surface. These results justify maintaining the natural pH of the manganese acetate solution (5.8) for the main adsorption experiments, as this pH is close to the optimal while minimizing alterations to the system. Overall, the pH-dependent study demonstrates that 24Nb100 exhibits stable and effective Mn^{2+} removal at pH 6.0. In contrast, deviations toward more acidic or more alkaline conditions reduce adsorption efficiency due to proton competition or metal hydroxide precipitation, respectively. Figure 7c presents Mn^{2+} adsorption as a function of Nb_2O_5 concentration. The influence of Nb_2O_5 particle concentration on metal ion adsorption has been investigated, and increasing the adsorbent concentration can enhance heavy metal adsorption due to a larger available surface area for adsorbent–solute interactions [11]. However, very high particle concentrations may hinder adsorption by promoting particle collisions and agglomeration. Under the conditions studied, 2.0 g L^{-1} particles achieved the highest adsorption (76%). Therefore, 2.0 g L^{-1} was selected for the subsequent study on contact time variation (Fig. 7d). Adsorption occurred rapidly during the first minute of contact, with approximately 78% of Mn^{2+} ions removed by Nb_2O_5, and equilibrium was reached quickly. Figure 8a illustrates this behavior in the Q_t-versus-time plot, showing a steep initial increase followed by a gradual leveling off until stabilization. Equilibrium between adsorption and desorption was observed within 10 min; however, experiments were extended to 60 min to confirm system stability. The

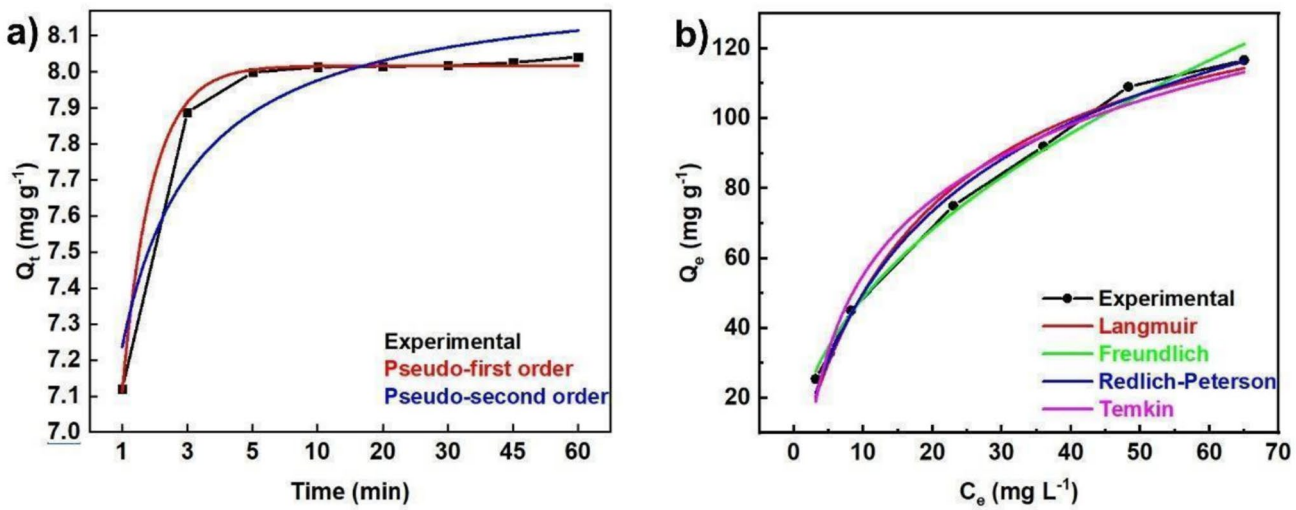

Figure 8 **a** Nonlinear fittings of pseudo-first-order and pseudo-second-order model for the experimental isotherm and **b** Nonlinear fittings of Langmuir, Freundlich, Redlich–Peterson, and Temkin isotherms for Mn^{2+} on sample 24Nb100.

Table 3 Kinetic parameters for Mn^{2+} adsorption on Nb_2O_5 subjected to hydrothermal treatment at 100 °C for 24 h (24Nb100)

	Q_e (mg g^{-1})	K (g min mg^{-1})	R^2
Pseudo-first-order model	8.0	2.2	0.99
Pseudo-second-order model	8.2	0.9	0.88

constant Mn^{2+} concentration after equilibrium demonstrates the robustness of the adsorption process, indicating that the material reaches its maximum capacity and maintains stable conditions over time, which is essential for practical applications. To confirm the adsorption kinetic model, the experimental data were fitted to pseudo-first-order and pseudo-second-order models. Figure 8a shows the curves of the fitted models compared to the experimental data, allowing validation of the adopted kinetic model.

The parameters of the pseudo-first-order and pseudo-second-order models, including the equilibrium adsorption capacity (Q_e) and the adsorption rate constants (k), were determined. The determination coefficient (R^2) was also calculated for each model, as shown in Table 3. Inspection of the correlation coefficients and the fit of each model to the experimental data revealed that the pseudo-first-order model provided a superior fit. The R^2 value of 0.99 indicates an excellent fit, close to the ideal value of 1. The adsorption capacity calculated from the pseudo-first-order model was 8.017 mg g^{-1}, in excellent agreement with the experimental value (8.042 mg g^{-1}), showing a negligible difference of only 0.3%.

The evaluation of kinetic models is essential for understanding the adsorption mechanism and predicting system behavior. In this study, the pseudo-first-order model provided the best fit, reflecting its assumption that the adsorption rate is proportional to the concentration of Mn^{2+} ions in solution. This suggests that the adsorption of Mn^{2+} on Nb_2O_5 is predominantly governed by the availability of active sites and physisorption rather than chemisorption, as described by the pseudo-second-order model involving electron sharing or exchange. The high surface area of Nb_2O_5 contributes significantly to its adsorption capacity by providing numerous active sites, consistent with the experimentally observed high Q_e values. Similar trends have been reported in the literature, where Ho and McKay [39] and Lagergren [41] showed that the pseudo-first-order model often better describes adsorption dominated by physical interactions. The close agreement between the experimental and calculated adsorption capacities (0.03 mg g^{-1}) confirms the reliability of this model for predicting Mn^{2+} uptake, which is crucial for designing and optimizing practical systems. These results indicate that Nb_2O_5 is an efficient adsorbent for Mn^{2+} removal, with rapid kinetics and predictable behavior, facilitating the optimization of contact time, adsorbent dosage, and metal ion concentration in water treatment and environmental remediation applications.

The adsorption isotherm was studied by varying Mn^{2+} concentrations to 10, 15, 20, 50, 75, and 100 mg L^{-1}. Figure 8b illustrates the fits made for isotherm models. The adsorption behavior of Mn^{2+} ions onto Nb_2O_5 was evaluated using the Langmuir, Freundlich, Temkin, and Redlich–Peterson isotherm models to elucidate the nature of the surface interactions and adsorption mechanism. The fitting parameters obtained from nonlinear regression are summarized in Table 4. The Langmuir model yielded a maximum adsorption capacity (Q_{max}) of 148.9 mg g^{-1}, indicating

Table 4 Langmuir, Freundlich, Redlich–Peterson, and Temkin isotherms for Mn^{2+} on sample 24Nb100

Model	Parameters
Langmuir	
Q_{max} (mg g^{-1})	148.9
K_L (L mg^{-1})	0.05
R^2	0.988
χ^2	4.52
Freundlich	
K_F ((mg g^{-1})(L mg^{-1}))$^{1/n}$	15.9
n	2
R^2	0.993
χ^2	0.56
Temkin	
A_T (L g^{-1})	0.6
B (kJ mol^{-1} L^{-1})	30.9
R^2	0.982
χ^2	0.98
Redlich–Peterson	
K_R (L g^{-1})	8.8
a_R (L mg^{-1})^g	0.1
g	0.88
R^2	0.993
χ^2	0.52

a high affinity of Nb_2O_5 toward Mn^{2+} ions. At the same time, the relatively low Langmuir constant ($K_L = 0.05$ L mg^{-1}) suggests moderate binding energy between the adsorbate and the surface. Although the Langmuir model assumes monolayer adsorption on a homogeneous surface with identical sites, the fit quality ($R_2 = 0.988$, $\chi^2 = 4.52$) shows that it only partially describes the adsorption process, indicating surface heterogeneity or the coexistence of multiple adsorption mechanisms.

Both the Freundlich and Redlich–Peterson models provided superior fits to the experimental data, reflecting a mixed adsorption mechanism. The Freundlich model exhibited $R^2 = 0.993$ and $\chi^2 = 0.56$, with a Freundlich constant $K_F = 15.9$ ((mg g^{-1})(L $mg^{-1})^{1/n}$) and heterogeneity factor n = 2, indicating favorable adsorption and a non-uniform distribution of active sites. The Redlich–Peterson model, a hybrid isotherm combining features of Langmuir and Freundlich, also showed excellent agreement ($K_R = 8.8$ L g^{-1}, $a_R = 0.1$ L mg^{-1}, $g = 0.88$, $R^2 = 0.993$, $\chi^2 = 0.52$). The exponent g, which is close to but less than unity, indicates that adsorption does not strictly follow ideal Langmuir behavior and instead exhibits Freundlich-type heterogeneity. The Temkin model, which accounts for adsorbate–adsorbent interactions and assumes a linear decrease in adsorption heat with surface coverage, also presented reasonable agreement ($R^2 = 0.982$, $\chi^2 = 0.98$). The Temkin constant B = 30.9 kJ mol^{-1} L^{-1} indicates moderate interaction strength, consistent with weak interactions rather than strong chemisorption. However, its inferior fit relative to the Freundlich and Redlich–Peterson models suggests that adsorbate–adsorbate interactions are not the primary driving force. Overall, these results indicate that Mn^{2+} adsorption on Nb_2O_5 occurs on energetically heterogeneous surfaces, involves multilayer formation, and is dominated by physical interactions, with the Freundlich and Redlich–Peterson models best capturing this mixed adsorption behavior.

To provide a clearer benchmark for comparison and to contextualize adsorption capacities of oxide-based materials, reported maximum Mn^{2+} uptake values (Q_{max}) for various metal oxide adsorbents are summarized in Table 5.

Table 5 compares the maximum adsorption capacities reported for various metal oxide-based adsorbents toward Mn^{2+} removal. Simple MnO-based systems, such as MnO–Coated hollow polymethylmethacrylate spheres, exhibit relatively low capacity (8.37 mg g^{-1}) under Langmuir fitting. Supported manganese oxide on zeolite (MnO_x/zeolite) shows an intermediate capacity (73.0 mg g^{-1}) with behavior fitting both Langmuir and Freundlich models. In comparison, magnetite–maghemite nanocomposites reach higher values (79.36 mg g^{-1}) under Langmuir assumptions. Dried MnO_x demonstrates significant uptake (125.7 mg g^{-1}). Notably, the Nb_2O_5 adsorbent obtained in this work exhibited a high Mn^{2+} adsorption capacity (116.67 mg g^{-1}), surpassing most previously reported metal oxide-based materials and highlighting its strong potential for efficient divalent metal ion removal.

For a better understanding of adsorption mechanisms and to investigate the role of surface functionalities in the adsorption mechanism, FTIR spectra were collected before and after the Mn^{2+} adsorption process. These results are presented in Fig. 9d. After adsorption, a noticeable shift in the C = O stretching band was observed, indicating an interaction between Mn^{2+} ions and carbonyl-containing surface groups. This band displacement suggests the involvement of these functional groups in the adsorption mechanism via surface complexation, indicating a contribution from localized chemisorption processes.

To further assess the influence of synthesis-derived surface groups, the material was thermally treated at 300 °C to reduce carbonyl and oxalate-related functionalities. The effectiveness of this treatment was

Table 5 Maximum Adsorption Capacities (Q_{max}) of Metal Oxide-Based Adsorbents for Mn^{2+}

Adsorbent (metal oxide base)	Q_{max} (mg g^{-1})	Isotherm model	References
MnO–Coated hollow polymethylmethacrylate	8.4	Langmuir	[42]
Magnetite–maghemite nanocomposite (Fe/Mn oxide)	79.4	Langmuir	[43]
Activated carbon with Fe/Mn oxide	49.7	Langmuir	[44]
Manganese oxide-coated zeolite (MnOx/zeolite)	73.0	Langmuir/Freundlich	[45]
MnO_x (dried manganese oxide)	125.7	Experimental	[46]
Nb_2O_5	116.67	Experimental	Our work

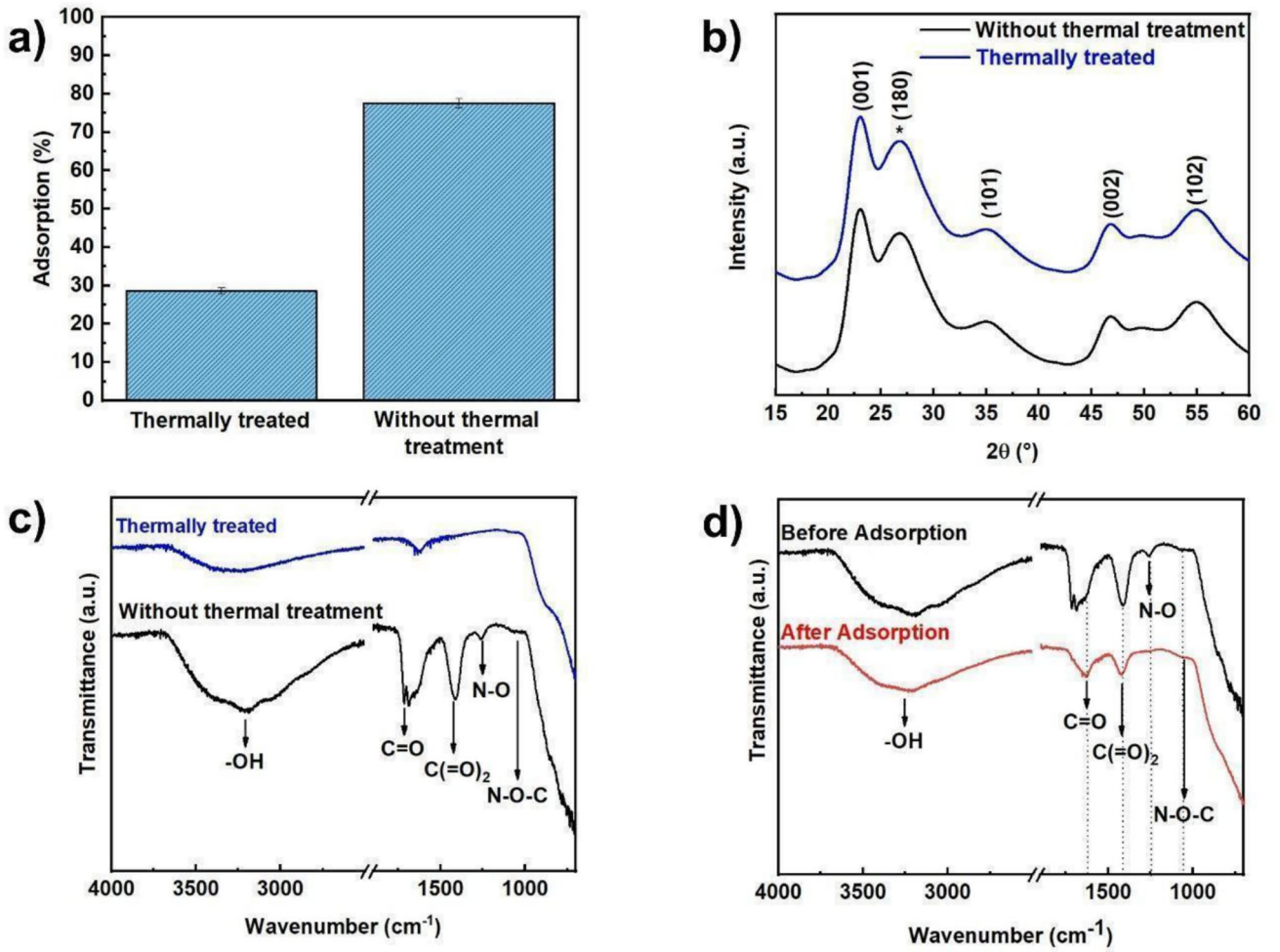

Figure 9 Influence of thermal treatment and surface chemistry on Mn^{2+} adsorption by Nb_2O_5: **a** Mn^{2+} adsorption efficiency before and after thermal treatment at 300 °C, **b** XRD patterns showing preservation of the Nb_2O_5 crystalline structure after thermal treatment, **c** FTIR spectra before and after thermal treatment, indicating removal of synthesis-derived surface groups, **d** FTIR spectra before and after Mn^{2+} adsorption, showing band shifts associated with interactions between Mn^{2+} and surface oxygen-containing species.

confirmed by FTIR analysis, which showed the disappearance of the corresponding absorption bands. Adsorption experiments performed with the thermally treated material revealed a pronounced decrease in Mn^{2+} removal efficiency, from 77.56% for the untreated sample to 28.56% after thermal treatment (Fig. 9a). This significant reduction demonstrates that surface functional groups generated during synthesis play a key role in defining active adsorption sites. In fact, the XRD diffractogram (Fig. 9b) shows that there was no change in the crystalline structure of the material when heated to 300 °C. This result demonstrates that the adsorptive properties are indeed linked to the surface groups.

The kinetic data were best described by the pseudo-first-order (PFO) model, indicating that the overall adsorption rate is predominantly controlled by physical interactions and mass transfer processes rather than by surface chemical reactions. This behavior suggests that although chemical interactions are present, they do not constitute the rate-limiting step in the adsorption process. Equilibrium data were better fitted by the Freundlich and Redlich–Peterson isotherm models, reflecting the heterogeneous nature of the Nb_2O_5 surface and the presence of adsorption sites with different energies. In particular, the Redlich–Peterson model, with a β value lower than unity, indicates a non-ideal adsorption behavior combining features of

both Langmuir- and Freundlich-type mechanisms, consistent with a mixed adsorption process.

Although Mn^{2+} adsorption also involves electrostatic interactions and coordination with inorganic hydroxyl groups associated with the oxide surface, the combined kinetic, isotherm, and spectroscopic results clearly indicate that synthesis-derived functional groups significantly enhance Mn^{2+} uptake. Overall, these results demonstrate that both inorganic hydroxyl sites and synthesis-derived functional groups contribute synergistically to a heterogeneous adsorption mechanism governed by physically controlled kinetics and localized chemical interactions.

Conclusion

Hydrothermally treated Nb_2O_5 synthesized via the oxidant peroxo method exhibited mesoporosity, and negatively charged, hydroxylated surfaces under mild synthesis conditions. Although increasing hydrothermal treatment time reduced the BET surface area, it promoted a more accessible pore architecture, which proved decisive for Mn^{2+} adsorption. The sample treated for 24 h showed the highest adsorption efficiency, demonstrating that pore accessibility and effective internal volume govern adsorption performance more strongly than surface area alone. Mn^{2+} adsorption was rapid, reaching equilibrium within minutes. Kinetic data were best described by the pseudo-first-order model, indicating that physical interactions and mass transfer predominantly control the process. Equilibrium data were better fitted by the Freundlich and Redlich–Peterson isotherms, revealing surface heterogeneity and a mixed adsorption mechanism. FTIR analyses before and after adsorption, together with thermal treatment experiments, demonstrated that synthesis-derived surface functional groups play a key role in Mn^{2+} uptake, while the crystalline structure remains unchanged. This study demonstrates that surface chemistry and pore accessibility are critical parameters for optimizing Mn^{2+} adsorption on Nb_2O_5, providing fundamental insights for the rational design of oxide adsorbents for heavy metal removal.

Acknowledgements

The authors thank the Brazilian research funding agencies Foundation Coordination for the Improvement of Higher Education Personnel (CAPES; Finance code 001), National Council for Scientific and Technological Development (CNPq), Minas Gerais State Research Support Foundation (FAPEMIG), São Paulo State Research Support Foundation (FAPESP; Process number 2023/08424-6), and Financier of Studies and Projects (FINEP) for their financial and technical support. They are also grateful to the Instrumentation Brazilian Agricultural Research Company (São Carlos, São Paulo, Brazil) and CBMM (Brazilian Metallurgy and Mining Company) for donating the ammonium niobium oxalate.

Funding

The Article Processing Charge (APC) for the publication of this research was funded by the Coordenação de Aperfeiçoamento de Pessoal de Nível Superior - Brasil (CAPES) (ROR identifier: 00x0ma614). Coordination for the Improvement of Higher Education Personnel, 001, Allef Leite, National Council for Scientific and Technological Development, Minas Gerais State Research Support Foundation, Financier of Studies and Projects, Fundação de Amparo à Pesquisa do Estado de São Paulo, 2023/08424-6, Allef Leite.

Data availability

The data that support the findings of this study are available from the corresponding author upon reasonable request.

Declarations

Conflict of interest The authors declare no competing interests.

Ethical approval Not applicable.

Consent to participate Not applicable.

Consent to publish All authors agree to publish.

Supplementary Information The online version contains supplementary material available at https://doi.org/10.1007/s10853-026-12458-9.

References

[1] Tanabe K (2003) Catalytic application of niobium compounds. Catal Today 78:65–77. https://doi.org/10.1016/S0920-5861(02)00343-7

[2] Guerrero-Pérez MO (2020) The fascinating effect of niobium as catalytic promoting agent. Catal Today 354:19–25. https://doi.org/10.1016/j.cattod.2019.04.008

[3] Taques Tractz G, Staciaki da Luz F, Regina Masetto Antunes S et al (2021) Nb_2O_5 synthesis and characterization by Pechini method to the application as electron transport material in a solar device. Sol Energy 216:1–6. https://doi.org/10.1016/j.solener.2021.01.029

[4] Mokrushin AS, Simonenko TL, Simonenko NP et al (2021) Chemoresistive gas-sensing properties of highly dispersed Nb_2O_5obtained by programmable precipitation. J Alloys Compd 868:159090. https://doi.org/10.1016/j.jallcom.2021.159090

[5] Suresh S, Deepak TG, Ni C et al (2016) The role of crystallinity of the $Nb_2 O_5$ blocking layer on the performance of dye-sensitized solar cells. New J Chem 40:6228–6237. https://doi.org/10.1039/C6NJ01133K

[6] Ong GK, Saez Cabezas CA, Dominguez MN et al (2020) Electrochromic niobium oxide nanorods. Chem Mater 32:468–475. https://doi.org/10.1021/acs.chemmater.9b04061

[7] Qu X, Liu Y, Li B et al (2020) Nanostructured T-Nb_2O_5-based composite with reduced graphene oxide for improved performance lithium-ion battery anode. J Mater Sci 55:13062–13074. https://doi.org/10.1007/s10853-020-04910-1

[8] Kim K, Hwang J, Seo H et al (2019) Surface-controlled Nb_2O_5 nanoparticle networks for fast Li transport and storage. J Mater Sci 54:2493–2500. https://doi.org/10.1007/s10853-018-3010-0

[9] Kozlovskiy A, Egizbek K, Zdorovets MV et al (2020) Evaluation of the efficiency of detection and capture of manganese in aqueous solutions of $FeCeO_x$ nanocomposites doped with Nb_2O_5. Sensors 20:4851. https://doi.org/10.3390/s20174851

[10] Li S, Zhang J, An H et al (2021) Preparation and catalytic performance of NiO-MnO_2/Nb_2O_5-TiO_2 for one-step synthesis of 2-ethylhexanol from n-butyraldehyde. Catal Commun 149:106250. https://doi.org/10.1016/j.catcom.2020.106250

[11] Zhang P, Wang M, Wang J et al (2018) Facile synthesis and characterization of low crystalline Nb_2O_5 ultrafine nanoparticles as a new efficient photocatalyst. J Non-Cryst Solids 500:371–376. https://doi.org/10.1016/j.jnoncrysol.2018.08.026

[12] Rodrigues T, Falsetti PHE, Del Duque DMS et al (2021) A versatile Nb_2O_5 /SnO_2 heterostructure for different environmental purposes: water treatment and artificial photosynthesis. ChemCatChem 13:730–738. https://doi.org/10.1002/cctc.202001569

[13] Zhou Y, Su B, Ren S et al (2021) Nb_2O_5-modified Mn-Ce/AC catalyst with high $ZnCl_2$ and SO_2tolerance for low-temperature NH_3-SCR of NO. J Environ Chem Eng 9:106323. https://doi.org/10.1016/j.jece.2021.106323

[14] Lopes OF, Paris EC, Ribeiro C (2014) Synthesis of Nb_2O_5 nanoparticles through the oxidant peroxide method applied to organic pollutant photodegradation: a mechanistic study. Appl Catal B Environ 144:800–808. https://doi.org/10.1016/j.apcatb.2013.08.031

[15] Sall ML, Diaw AKD, Gningue-Sall D et al (2020) Toxic heavy metals: impact on the environment and human health, and treatment with conducting organic polymers, a review. Environ Sci Pollut Res Int 27:29927–29942. https://doi.org/10.1007/s11356-020-09354-3

[16] Rahman Z (2020) An overview on heavy metal resistant microorganisms for simultaneous treatment of multiple chemical pollutants at co-contaminated sites, and their multipurpose application. J Hazard Mater 396:122682. https://doi.org/10.1016/j.jhazmat.2020.122682

[17] Kan C-C, Aganon MC, Futalan CM, Dalida MLP (2013) Adsorption of Mn^{2+} from aqueous solution using Fe and Mn oxide-coated sand. J Environ Sci (China) 25:1483–1491. https://doi.org/10.1016/S1001-0742(12)60188-0

[18] Fikri E, Mutiara Farid R, Septiati Y et al (2022) Effect of zeolite and activated carbon thickness variation as adsorbent media in reducing phenol and manganese levels in wastewater of non-destructive testing unit. J Ecol Eng 23:40–48. https://doi.org/10.12911/22998993/150653

[19] Radoykova TH, Dimitrova SV, Aleksieva KI, et al Comparative Mn^{2+} adsorption on waste lignocellulosic materials

[20] Uzcan F, Isak AA, Soylak M (2025) Nb_2O_5@PVP as an efficient adsorbent for the dispersive micro solid phase extraction of lead (II) ions in pet food and wastewater samples. J Food Compos Anal 146:107932. https://doi.org/10.1016/j.jfca.2025.107932

[21] Wang G, Yan T, Shen J et al (2021) Beneficial synergy of adsorption–intercalation–conversion mechanisms in Nb_2O_5@nitrogen-doped carbon frameworks for promoted removal of metal ions via hybrid capacitive deionization. Environ Sci Nano 8:122–130. https://doi.org/10.1039/D0EN01003K

[22] Rianjanu A, Marpaung KDP, Melati EKA et al (2024) Integrated adsorption and photocatalytic removal of methylene blue dye from aqueous solution by hierarchical Nb_2O_5@PAN/PVDF/ANO composite nanofibers. Nano Materials Science 6:96–105. https://doi.org/10.1016/j.nanoms.2023.10.006

[23] Leite Dos Santos A, Almeida Dias J, Tiago Dos Santos Tavares G et al (2023) Niobium pentoxide as an adsorbent for methylene blue removal: synthesis, characterization and thermal stability. Mater Chem Phys 301:127659. https://doi.org/10.1016/j.matchemphys.2023.127659

[24] Anderson JS, Hutchison JL, Lincoln FJ (1997) Dislocations and related defects in niobium oxide structures. Proc Royal Soc London A Math Phys Sci 352:303–323. https://doi.org/10.1098/rspa.1977.0001

[25] Jia Y, Zhong M, Yang F et al (2020) Theoretical and experimental study on exciton properties of TT-, T-, and H-Nb_2O_5. J Phys Chem C 124:15066–15075. https://doi.org/10.1021/acs.jpcc.0c04202

[26] Ücker CL, Goetzke V, Almeida SR et al (2021) Photocatalytic degradation of rhodamine B using Nb_2O_5 synthesized with different niobium precursors: factorial design of experiments. Ceram Int 47:20570–20578. https://doi.org/10.1016/j.ceramint.2021.04.066

[27] Giraldi TR, Costa da BC, Silva MM et al (2023) Nb_2O_5 pellets with inactive biomass for adsorption of Mn^{2+} ions: kinetic, isothermal and reuse study. Mater Res 26:e20220553. https://doi.org/10.1590/1980-5373-MR-2022-0553

[28] Uekawa N, Kudo T, Mori F et al (2003) Low-temperature synthesis of niobium oxide nanoparticles from peroxo niobic acid sol. J Colloid Interface Sci 264:378–384. https://doi.org/10.1016/S0021-9797(03)00460-0

[29] Holzwarth U, Gibson N (2011) The Scherrer equation versus the "Debye-Scherrer equation." Nat Nanotechnol 6:534–534. https://doi.org/10.1038/nnano.2011.145

[30] Pinto AH, Nogueira AE, Gonçalves MD, Camargo ER (2021) Fundamentals and Advances of the Oxidant Peroxo Method (OPM) for the Synthesis of Transition Metal Oxides. In: La Porta FA, Taft CA (eds) Functional Properties of Advanced Engineering Materials and Biomolecules. Springer International Publishing, Cham, pp 109–154

[31] Bindu P, Thomas S (2014) Estimation of lattice strain in ZnO nanoparticles: X-ray peak profile analysis. J Theor Appl Phys 8:123–134. https://doi.org/10.1007/s40094-014-0141-9

[32] Gupta VK, Nayak A (2012) Cadmium removal and recovery from aqueous solutions by novel adsorbents prepared from orange peel and Fe_2O_3 nanoparticles. Chem Eng J 180:81–90. https://doi.org/10.1016/j.cej.2011.11.006

[33] Largitte L, Pasquier R (2016) A review of the kinetics adsorption models and their application to the adsorption of lead by an activated carbon. Chem Eng Res Des 109:495–504. https://doi.org/10.1016/j.cherd.2016.02.006

[34] Langmuir I (1918) The adsorption of gases on plane surfaces of glass, mica and platinum. J Am Chem Soc 40:1361–1403. https://doi.org/10.1021/ja02242a004

[35] Borys P, Grzywna ZJ (2016) On the fractality of the Freundlich adsorption isotherm in equilibrium and non-equilibrium cases. Phys Chem Chem Phys 18:20784–20789. https://doi.org/10.1039/C6CP03356C

[36] Raji Z, Karim A, Karam A, Khalloufi S (2023) Adsorption of heavy metals: mechanisms, kinetics, and applications of various adsorbents in wastewater remediation—a review. Waste 1:775–805. https://doi.org/10.3390/waste1030046

[37] Ko EI, Weissman JG (1990) Structures of niobium pentoxide and their implications on chemical behavior. Catal Today 8:27–36. https://doi.org/10.1016/0920-5861(90)87005-N

[38] Brunauer S, Deming LS, Deming WE, Teller E (1940) On a theory of the van der Waals adsorption of gases. J Am Chem Soc 62:1723–1732. https://doi.org/10.1021/ja01864a025

[39] Ho YS, Ng JCY, McKay G (2000) Kinetics of pollutant sorption by biosorbents: review. Sep Purif Methods 29:189–232. https://doi.org/10.1081/SPM-100100009

[40] Martínez Casillas DC, Longinotti MP, Bruno MM et al (2018) Diffusion of water and electrolytes in mesoporous silica with a wide range of pore sizes. J Phys Chem C 122:3638–3647. https://doi.org/10.1021/acs.jpcc.7b11555

[41] Lagergren S (1898) About the theory of so called adsorption of soluble substances. About the Theory of so Called Adsorption of Soluble Substances 1–39

[42] Dutta D, Borah JP, Puzari A (2021) Adsorption of Mn^{2+} from aqueous solution using manganese oxide-coated hollow

polymethylmethacrylate microspheres (MHPM). Adsorpt Sci Technol 2021:5597299. https://doi.org/10.1155/2021/5597299

[43] Siddiqa A, Khatun MostH MostH, Mostafa MG (2025) Adsorption of Mn(II) on green-synthesized magnetite-maghemite nanocomposite adsorbents: kinetic, equilibrium, and thermodynamic studies. Appl Water Sci 15:280. https://doi.org/10.1007/s13201-025-02622-y

[44] Elewa A, Amer A, Attalah M, Gad H (2021) Removal of some heavy metals contaminants from aqueous solutions by applying biomass-based modified activated carbon. Egypt J Chem 0:0–0. https://doi.org/10.21608/ejchem.2021.72070.3600

[45] Taffarel SR, Rubio J (2010) Removal of Mn^{2+} from aqueous solution by manganese oxide coated zeolite. Miner Eng 23:1131–1138. https://doi.org/10.1016/j.mineng.2010.07.007

[46] Zhang R, Yang L, Yang J et al (2025) Effects of drying operation on the Mn^{2+} removal activity of MnO_x: performance and mechanism. Water 17:261. https://doi.org/10.3390/w17020261